

# Structure Formation, Melting, and the Optical Properties of Gold/DNA Nanocomposites: Effects of Relaxation Time

Sung Yong Park and D. Stroud

*Department of Physics, The Ohio State University, Columbus, Ohio 43210*

(October 29, 2018)

We present a model for structure formation, melting, and optical properties of gold/DNA nanocomposites. These composites consist of a collection of gold nanoparticles (of radius 50 nm or less) which are bound together by links made up of DNA strands. In our structural model, the nanocomposite forms from a series of Monte Carlo steps, each involving reaction-limited cluster-cluster aggregation (RLCA) followed by dehybridization of the DNA links. These links form with a probability  $p_{eff}$  which depends on temperature and particle radius  $a$ . The final structure depends on the number of monomers (i. e. gold nanoparticles)  $N_m$ ,  $T$ , and the relaxation time. At low temperature, the model results in an RLCA cluster. But after a long enough relaxation time, the nanocomposite reduces to a compact, non-fractal cluster. We calculate the optical properties of the resulting aggregates using the Discrete Dipole Approximation. Despite the restructuring, the melting transition (as seen in the extinction coefficient at wavelength 520 nm) remains sharp, and the melting temperature  $T_M$  increases with increasing  $a$  as found in our previous percolation model. However, restructuring increases the corresponding link fraction at melting to a value well above the percolation threshold. Our calculated extinction cross section agrees qualitatively with experiments on gold/DNA composites. It also shows a characteristic “rebound effect,” resulting from incomplete relaxation, which has also been seen in some experiments. We discuss briefly how our results relate to a possible sol-gel transition in these aggregates.

## I. INTRODUCTION

The optical properties of metallic nanoparticles have been investigated intensively for many years [1,2]. Recently, this work has extended to so-called functional metallic nanoparticles, which may have a variety of novel and useful optical and mechanical properties [3]. Among these, there has been particular interest in the DNA-modified gold nanoparticle (gold/DNA nanocomposite) system. This is a material consisting of gold nanoparticles to which specific kinds of organic molecules (e. g., noncomplementary oligonucleotides capped with thiol groups) can be attached. These materials can be produced in a variety of structures using a strategy of nanoparticle self-assembly [4–8]. They may also be useful for selective biological detection, by making use of the optical and electrical sensitivity of their aggregates [9–14].

Numerical model calculations of the optical properties of DNA modified gold nanoparticle aggregates show general agreement with experiments. For example, both experiments and calculations show that (i) for isolated gold nanoparticles in suspension, there is a strong surface plasmon absorption in the visible, arising from oscillations of electronic charge in the gold nanoparticles; and (ii) this absorption maximum broadens and red-shifts when the cluster radius becomes comparable to the wavelength [15–17].

Although the DNA molecules absorb primarily in the ultraviolet, they nonetheless play a central role in the op-

tical properties of these aggregates in the visible, because they strongly influence the *structure* of the gold/DNA aggregates. For example, the DNA tends to form multiple links between individual gold nanoparticles. These multiple links appear to account for some key structural features of the aggregates [18–20]. In particular, the melting transition for a gold nanoparticle aggregate has a much narrower temperature width, and occurs at a substantially higher temperature  $T$ , than that of a single DNA duplex [9,21]. In addition, the presence of multiple links leads to a natural explanation for the dependence of the aggregate melting temperature, denoted  $T_M$  on particle size [20,22].

In the present work, we extend our previous model calculations [18,19] to take into account the *dynamics* of aggregate formation, and how these dynamics affect the aggregate optical properties. In our previous work, the melting of the aggregates was treated using a purely statistical criterion. Specifically, the aggregates were formed by removing DNA links between gold nanoparticles on a simple cubic lattice, with a suitable, temperature-dependent probability. In the limit of a large aggregate, the melting transition occurs, in this model, when the fraction of links falls below the percolation threshold  $p_c$  for the lattice considered. The calculated aggregate optical properties are found to change dramatically when this threshold is passed, in good agreement with experiment.

To improve on this approach, we describe below a model for structure formation which starts from isolated

gold nanoparticles. Our model takes into account two important features of the structure formation: the diffusion of nanoparticles, or clusters of nanoparticles, through the solvent to form a cluster, and the chemical reaction between DNA chains which produces the links between the nanoparticles.

Our structural model leads to a wide range of possible aggregate morphologies, depending on the temperature. Corresponding to these morphologies is a broad range of possible optical properties. In this paper, we will present numerical results for both the structural and optical properties of these nanocomposites over a typical range of parameters. For physically reasonable parameters, our numerical results are in good agreement with experiment. We will present a qualitative interpretation of these results, and compare them to our earlier, purely percolation model.

The remainder of this paper is organized as follows. In Section II, we describe our structural model for gold/DNA nanocomposites, and explain how it is implemented numerically. In Section III, we review the Discrete Dipole Approximation, which is the method used to calculate the optical properties of this system; we also discuss various technical details needed to treat the irregular clusters which emerge from the structural model of Section II. In Section IV, we present our numerical results for both the structural and the optical properties of the aggregates. Finally, in Section V, we summarize our results, interpret them in terms of the expected behavior of typical gold/DNA nanocomposites, compare our results to available experiments, and discuss their possible implications for future work.

## II. STRUCTURAL MODEL AND ITS NUMERICAL IMPLEMENTATION

In this Section, we describe our structural model for the formation of gold/DNA aggregates. We start by describing the expected aggregation behavior at low  $T$ . Following this, we present our full structural model and its numerical implementation for arbitrary  $T$ .

### A. Aggregation at Low $T$ .

Before discussing the aggregation of gold/DNA nanocomposites at low  $T$ , we first consider the aggregation behavior of other typical colloids, i. e. suspensions of small solid particles in a liquid solvent. As the individual colloidal particles stick together to become clusters, these clusters themselves diffuse through the solvent, and continue to collide and aggregate. This behavior is an example of cluster-cluster aggregation.

If bonding between two colloidal particles is irreversible, the final aggregate generally results from one

of two processes: reaction-limited aggregation (RLA) or diffusion-limited aggregation (DLA). If there is a repulsive energy barrier between two approaching colloidal particles, the resulting process is expected to be a reaction-limited aggregation, because the reaction barrier is the limiting step in cluster growth [23]. By contrast, if there were no barrier, the aggregation would be dominated by diffusion processes, and the resulting clusters should exhibit the features of DLA. DLA clusters, like RLA clusters, are fractals, but they have a substantially lower  $d_f$  than the RLA clusters. For forming both types of fractal clusters, however, the irreversibility of binding is important. Without irreversibility, the final cluster is likely to become compact and non-fractal [24,25].

We now provide a possible justification for considering the growth of the colloidal cluster in a dilute solution of DNA-modified gold particles at very low  $T$  as reaction-limited cluster-cluster aggregation (RLCA). Here, we should note that for the DNA-modified gold nanoparticle system, the mechanism for binding two DNA-modified gold nanoparticles differs from the ordinary colloid aggregation process discussed above, because binding can occur only if the DNA hybridizes, i. e., if the two DNA single strands on different gold particles and one linker single DNA strand undergo a reversible chemical reaction to form a double strand. However, for two reasons, RLCA may still be a plausible growth mechanism for the gold cluster aggregation in a dilute solution at very low  $T$ . First, at the very low  $T$ , once the DNA hybridization occurs and the two gold particles do stick together, they rarely unbind, since thermal fluctuation cannot provide enough energy to break them apart. Thus, the aggregation process is *irreversible*. Secondly, in case of DNA hybridization, this reaction barrier can actually be experimentally observed [26]. Because of this barrier, nanoparticles must collide numerous times before two particles can stick together, since DNA hybridization takes a finite time.

As  $T$  increases, the above argument, based on the irreversible binding, is no longer valid, since DNA dehybridization may easily take place. Thus, the restructuring of clusters is crucial for understanding the cluster morphology and the melting transition. We now describe a structural model which includes the effects of this restructuring on the cluster morphology.

### B. Model for Structure Formation at General Temperature

#### 1. Description of the Model

At finite  $T$ , cluster restructuring is sensitive to the relative magnitudes of two times scales, which we denote  $\tau_{bind}$  and  $\tau_{dehyb}$ .  $\tau_{bind}$  is the time elapsed when two clusters meet and attempt to form a link, while  $\tau_{dehyb}$  is the

time needed for a a double DNA strand to dehybridize into two single DNA strands under the influence of thermal fluctuations. At low T,  $\tau_{dehyb} \gg \tau_{bind}$  [26]. Hence, there will be many cluster-cluster binding events in the time required for a one dehybridization. In the present model, we will assume that  $\tau_{dehyb} \gg \tau_{bind}$  at *all* T. With this assumption, we can consider aggregation and dehybridization processes separately. That is, we can establish a model in which, first the monomers undergo aggregation and form one single large cluster, and, next, the cluster breaks into smaller parts via a suitable cluster unbinding process due to DNA dehybridization [27].

Our aggregation procedure is carried out by a model of RLCA [28], as justified in the previous subsection. In this algorithm, the system is assumed to be made up initially of a large number  $N_m$  of “monomers” (each consisting of a single gold nanosphere of radius  $a$ ). In the first step of the aggregation, we choose two monomers at random, then place them at two different points chosen randomly on the sites of a simple cubic lattice of lattice constant  $\ell$  and edge  $L \equiv N\ell$  in  $d$  dimensions ( $d = 3$  in all of our simulations), with free boundary conditions. If the particles happen to be placed on adjacent sites, they are assumed to form a two-particle cluster, and are removed from the lattice. If they are placed on non-adjacent sites, the procedure is repeated until they do form a cluster. In the next step, two of the  $N_m - 1$  clusters, chosen at random, are placed in random, but non-overlapping positions and random orientations on the lattice. If they are adjacent, the two clusters are assumed to merge and form a larger cluster; otherwise, the procedure is repeated until the number of clusters is again reduced by one. In the  $n^{th}$  step, the same procedure is carried with two clusters randomly chosen from the now  $N_m - n + 1$  clusters. Eventually, this procedure leads to the formation of a single large cluster.

Once our aggregation procedure is finished, the next step in the procedure is to simulate cluster unbinding due to DNA dehybridization. Here we use a percolation algorithm, where the key parameter is  $p_{eff}$ , the probability that a given link between two monomers in the cluster remains the same without breaking. Note that this  $p_{eff}$  is obviously related to DNA hybridization, and thus depends on temperature. (The exact relation of  $p_{eff}$  to DNA hybridization is discussed in the next subsection.) With probability  $1 - p_{eff}$ , we randomly remove links in the cluster, which has formed from the aggregation procedure. After random removal of links, the cluster may separate several clusters, and thus we use a simple computer algorithm in order to identify the separate clusters [30]. If the resulting aggregate consists of two or more clusters, these aggregates are placed in random, but non-overlapping, positions and orientations on the large cubic lattice. This configuration will be used for the calculation of optical properties.

The two procedures described above are defined as one

single Monte Carlo (MC) “step.” To generate the final configuration, we carry out a series of  $N_{MC}$  MC steps, each involving aggregation and cluster unbinding. The end result is one or more final clusters.

The structure and the number of the final cluster or clusters depend on  $p_{eff}$ . If  $p_{eff} = 1$ , the final result is simply a single cluster formed from the aggregation part of the first MC step, which for large enough  $N_m$ , is known to be a RLCA fractal, with fractal dimension  $d_f = 2.1$  if  $d = 3$  [28]. For  $p_{eff} < 1$ , two types of transitions can take place in this system: a “sol-gel transition” and a “melting transition.” If  $p_{eff}$  is slightly less than 1, the restructuring of cluster does occur and tends to make the cluster more compact, and it may eventually become non-fractal at a certain  $p$ , denoted  $p_{SG}$ . We can call this transition as “sol-gel” transition [29]; for  $p > p_{SG}$ , the system will be a “gel,” i. e., a fractal cluster, while for  $p < p_{SG}$ , it will be “sol,” characterized by compact and non-fractal clusters. If  $p_{eff}$  is substantially smaller than 1, there are no longer large aggregation clusters. Thus we can define the “melting transition” as the point where, even in the limit of very large  $N_m$ , the aggregation procedure described above leads only to finite clusters - there is no “infinite cluster.” This transition occurs at a critical value of  $p_{eff}$ , denoted  $p_M$ . If there is no restructuring effect, this transition is related to the bond percolation transition, and thus we can consider that  $p_M = p_c$ , where  $p_c$  is the bond percolation threshold (for example,  $p_c \sim 0.25$  on a 3-dimensional simple cubic lattice) [30]. Next, we discuss the connection between  $p_{eff}$  and the physical parameters of the real gold/DNA nanoparticle system, as previously analyzed in Ref. [18].

## 2. Determination of $p_{eff}$ by DNA hybridization

At a low temperature T, a “link” is expected to consist of a number, say  $N_d$ , of DNA “duplexes,” i. e., of pairs of DNA strands connected to form a molecule. In actuality, there is a linker molecule which emerges from solution to connect two DNA single strands, each on a different nanoparticle. Even in this case, however, the melting condition can be reduced to that used here, without loss of accuracy, as will be shown in Ref. [19]. Also, there are actually two chemically distinct DNA single strands (denoted A and B); each gold particle has either all A or all B single strands attached, and the linker molecule can connect only A and B single strands. The existence of two species can be disregarded by symmetry when the concentrations of the two species in solution are equal; experiments have been carried out only under these conditions [4,9,17,20,22].

Thus, we simply assume that each DNA duplex consists of one double strand D, made up of two short single strands S (each having 12-14 DNA base pairs). To describe DNA dehybridization, we adopt a simple two-state

model [26,31]. There also exists a more elaborate theory which can account for many detailed features of the gold/DNA nanocomposite, including the dependence of the melting transition temperature  $T_M$  on the salt concentration of the solvent [20]. However, as mentioned in Introduction, both theories reached the same qualitative conclusion about the melting transition, namely that the observed sharp melting transition and the melting temperature dependence on the system size originate from the presence of multiple DNA links between each pair of nanoparticles. Moreover, the simple model we use here can be easily extended to the similar systems discussed in Ref. [10,32–34].

In a simple two-state model, the relative proportion of D and S is determined by the chemical reaction



The chemical equilibrium condition corresponding to eq. (1) is

$$\frac{(1 - p(T))^2}{p(T)} = \frac{K(T)}{C_T}, \quad (2)$$

where  $p(T)$  is the fraction of the single DNA strands which form double strands by the reaction (1) at temperature  $T$ ,  $K(T)$  is a chemical equilibrium constant, and  $C_T$  is the molar concentration of single DNA strands in the sample, Since  $0 < p(T) < 1$ , the physical solution to eq. (2) is

$$p(T) = 1 + \frac{1}{2} \left( K' - \sqrt{K'^2 + 4K'} \right), \quad (3)$$

where  $K' = K(T)/C_T$ . Since  $K'(T)$  is typically an increasing function of  $T$ ,  $p(T)$  will generally decrease with increasing  $T$ . In our calculations, we have also assumed the simple van 't Hoff behavior

$$K(T) = \exp[-\Delta G/k_B T], \quad (4)$$

with a Gibbs free energy of formation

$$\Delta G(T) = c_1(T - T_M^0) + c_3(T - T_M^0)^3, \quad (5)$$

choosing the values of  $c_1$ ,  $c_3$ , and  $T_M^0$  to be consistent with experiments on these DNA molecules [35]. The temperature  $T_M^0$  can be interpreted as the melting temperature of a single DNA duplex.

Given  $p(T)$ ,  $1 - p_{eff}$  is the probability that *none* of the duplexes forms a double strand. If the duplexes react independently, this probability is simply

$$1 - p_{eff}(T) = [1 - p(T)]^{N_d/z}, \quad (6)$$

where  $N_d$  is the number of single strands on each monomer, and  $z$  is the number of nearest neighbors for the given lattice ( $z = 6$  for a simple cubic lattice). Thus,  $p_{eff}(T)$  is also a decreasing function of  $T$ , but for

$N_d \gg 1$  will typically vary much more sharply with  $T$  than  $1 - p(T)$ .

The criterion for the melting temperature  $T_M$  of the aggregate is easily written down for a fully occupied lattice. If we denote the melting probability by  $p_M \equiv p_{eff}(T_M)$ , the melting temperature for a periodic lattice of monomers is simply

$$1 - p_M = [1 - p(T_M)]^{N_d/z}. \quad (7)$$

Eq. (7) implicitly determines  $T_M$  in terms of  $p_M$ ,  $N_d$ , and  $z$ . As discussed in Ref. [18], if we assume that the specific links which are occupied at temperature  $T$  are time-independent, the melting takes place at  $p_M = p_c$ , where  $p_c$  is the bond percolation threshold for the lattice considered, at which an infinite connected path of double DNA strands first forms. For example,  $p_c \sim 0.25$  on a very large simple cubic lattice.

Note that, according to eq. (7),  $p(T_M)$  decreases with increasing  $N_d$  and, hence, with increasing particle radius, since  $N_d$  should be proportional to the surface area of a nanoparticle. To obtain specific values for  $T_M$ , we assume  $N_d \propto a^2$ , set  $z = 6$  and use the experimental result that  $N_d = 160$  when  $a = 8$  nm [36]. Since  $p(T)$  decreases monotonically with  $T$ ,  $T_M$  should thus *increase* monotonically with  $a$ , as reported in experiments [20,22].

In the present paper, we keep our structural model as simple as possible, so as to focus on the essential features of the aggregation process. In reality, there are many complicated issues which should be considered. For example, the binding of DNA to the gold nanoparticles is a statistical process [7], and thus there will always be a distribution in the number of DNA strands per particle. Moreover, because of the high local dielectric function arising from the large amount of DNA on the particles, not every DNA single strands which is bound on the particles can hybridize with the linker DNA [36]. Furthermore, it is unlikely that the gold/DNA composite resulting from the aggregation process will form a regular crystal. All these features could, however, be included in an extension of our theory.

### III. OPTICAL PROPERTIES

#### A. Discrete Dipole Approximation

Given the distribution of clusters, and their geometries, we calculate their optical properties as follows. We first assume that, at any given time  $t$ , the extinction coefficient  $C_{ext}(t)$  of a given cluster can be calculated as if none of the other clusters were present. This amounts to neglecting corrections due to multiple scattering among the different clusters. We calculate  $C_{ext}$  for each cluster using the so-called discrete dipole approximation (DDA), first proposed by Purcell and Pennypacker [37].

As originally formulated, the DDA permits one to calculate the extinction coefficient of an irregularly shaped object of complex, frequency-dependent dielectric constant  $\bar{\epsilon}(\omega)$ , embedded in a homogeneous medium of real dielectric constant  $\bar{\epsilon}_h$  and subjected to an applied electromagnetic wave with electric field  $\mathbf{E}_0 \exp(\mathbf{k} \cdot \mathbf{r} - \omega t) \equiv \mathbf{E}_0(\mathbf{r})e^{-i\omega t}$ . (In our notation, the physical field  $\mathbf{E}_{phys}(\mathbf{r}, t)$  is the real part of this complex quantity.) In the DDA, the object is replaced by a collection of  $N_{par}$  identical point objects with polarizability  $\alpha(\omega)$  placed on a simple cubic lattice having a suitable lattice constant  $d$ .

The relation between the polarizability  $\alpha$  of these point objects and  $\epsilon(\omega)$  is discussed in Section IIIB. The induced dipole moment  $\mathbf{p}_i$  of the  $i^{th}$  polarizable point object is expressed as

$$\mathbf{p}_i = \alpha \mathbf{E}_{loc,i}, \quad (8)$$

where  $\mathbf{E}_{loc,i}$ , the local electric field at the position of the  $i^{th}$  point dipole, is

$$\mathbf{E}_{loc,i} = \mathbf{E}_0 \exp[i\mathbf{k} \cdot \mathbf{r}_i - i\omega t] - \sum_{j \neq i} \mathbf{A}_{ij} \cdot \mathbf{p}_j. \quad (9)$$

Thus  $\mathbf{E}_{loc,i}$  is the sum of the applied field at  $\mathbf{r}_i$  and all the scattered fields  $-\mathbf{A}_{ij} \cdot \mathbf{p}_j$  emanating from the induced dipoles at  $\mathbf{r}_j$ . In the DDA, the product  $\mathbf{A}_{ij} \cdot \mathbf{p}_j$  can be expressed as [15,37,38]

$$\begin{aligned} \mathbf{A}_{ij} \cdot \mathbf{p}_j &= \frac{e^{ikr_{ij} - i\omega t}}{r_{ij}^3} \{k^2 \mathbf{r}_{ij} \times [(\mathbf{r}_{ij} \times \mathbf{p}_j) + \\ &+ \frac{1 - ikr_{ij}}{r_{ij}^2} [r_{ij}^2 \mathbf{p}_j - 3\mathbf{r}_{ij}(\mathbf{r}_{ij} \cdot \mathbf{p}_j)]]\}. \end{aligned} \quad (10)$$

Here  $\mathbf{r}_{ij} = \mathbf{r}_i - \mathbf{r}_j$  and  $k = \omega/c \equiv 2\pi/\lambda$ ,  $c$  being the speed of light in vacuum, and  $\lambda$  the wavelength in vacuum. Eqs. (8)-(10) form a coupled set of  $3N_{par}$  equations, which can be solved for the  $N_{par}$  dipole moments  $\mathbf{p}_i$  using the complex-conjugate gradient method combined with fast Fourier transforms [38]. Given the  $\mathbf{p}_i$ 's,  $C_{ext}$  for a given cluster is obtained from the relation

$$C_{ext} = \frac{4\pi k}{|\mathbf{E}_0|^2} \text{Im} \left[ \sum_{j=1}^{N_{par}} \mathbf{E}_0^* \exp(-i\mathbf{k} \cdot \mathbf{r}_j) \cdot \mathbf{p}_j \right], \quad (11)$$

where the sum runs over the  $N_{par}$  particles in the cluster.

## B. Dipole Polarizability

In the DDA, there are many possible choices for the relation between the polarizability  $\alpha(\omega)$  of the point objects and  $\bar{\epsilon}(\omega)$  [39]. One possible choice is to use the Clausius-Mossotti equation:

$$\bar{\epsilon}(\omega) - 1 = \frac{4\pi n\alpha}{1 - (4\pi/3)n\alpha}. \quad (12)$$

where  $n = 1/d^3$  is the number of point polarizable objects per unit volume. This relationship between  $\bar{\epsilon}(\omega)$  and  $\alpha$  is accurate for point polarizable objects on a cubic mesh, provided that the wavelength in the medium,  $\lambda_m$  is much larger than  $d$  [40]. However, if  $d/\lambda_m$  is not very small, this choice can violate the optical theorem. To prevent this violation, an extension of the Clausius-Mossotti equation to include a radiative reaction correction has been proposed [41]. For a simple cubic lattice, this correction can be incorporated by using a lattice dispersion relation, which is appropriate for a periodic cluster [42].

One can also choose  $\alpha$  by connecting it to the first scattering coefficient in the Mie theory, usually denoted  $a_1$ . If we take the ‘‘point dipole’’ as a sphere of radius  $a$ , dielectric constant  $\epsilon$ , in a host medium of dielectric constant  $\epsilon_h$ , then, as discussed in Ref. [43], the relation between  $\alpha$  and  $a_1$  is

$$\alpha = i \frac{3}{2k^3} a_1. \quad (13)$$

Here

$$a_1 = \frac{m\psi_1(mx)\psi_1'(x) - \psi_1(x)\psi_1'(mx)}{m\psi_1(mx)\xi_1'(x) - \xi_1(x)\psi_1'(mx)}, \quad (14)$$

where  $\psi_1(x) = xj_1(x)$  and  $\xi_1 = xh_1^{(1)}(x)$ , the complex number  $m = \sqrt{\epsilon(\omega)/\epsilon_h}$ , and  $x = 2\pi\sqrt{\epsilon}a/\lambda$ . Here  $j_1(x)$  is the usual first order spherical Bessel function, and  $h_1^{(1)}$  is the first order spherical Hankel function.

## C. Application of the DDA to the Gold/DNA Composite System

In the present work, each cluster consists of a number of DNA-linked individual gold nanoparticles. The application of DDA to this gold/DNA system clusters has been developed extensively for regular clusters [15,16]. In carrying out the calculations for irregular clusters, we do not explicitly include the optical properties of the DNA molecules, since these absorb primarily in the ultraviolet [17]. We use tabulated values for the complex index of refraction  $n_{bulk}(\omega)$  of bulk gold [44,45], then calculate  $C_{ext}$  for each cluster using the DDA, using a finite-particle-size corrected dielectric function for the gold particles,’’ denoted  $\epsilon(\omega)$ .

We obtain  $\epsilon(\omega)$  by correcting the bulk dielectric function  $\epsilon_{bulk}(\omega) = n_{bulk}^2(\omega)$  to account for the additional damping mechanism induced by collision of the conduction electrons with the particle surface. Specifically, we write

$$\epsilon(\omega) = \epsilon_{bulk}(\omega) + \frac{\omega_p^2}{\omega(\omega + i/\tau)} - \frac{\omega_p^2}{\omega + i/\tau + i/\tau_a}, \quad (15)$$

where  $\epsilon_{bulk}(\omega)$ ,  $\omega_p$ , and  $1/\tau$  are the experimental bulk metal values for the dielectric function, plasma angular frequency, and relaxation rate. The quantity

$$1/\tau_a = Av_F/a_{eff} \quad (16)$$

is the surface damping term.  $v_F$  is the Fermi velocity, and  $a_{eff}$  is an effective particle radius, defined by setting  $4\pi a_{eff}^3/3 = v_{part}$ , where  $v_{part}$  is the particle volume. (Obviously, this expression is exact for spherical particles.) The constants  $\omega_p$ ,  $\tau$ , and  $v_F$  are taken from Ref. [46]. The constant  $A$  is a theory-dependent parameter that includes details of the scattering process [47], and is expected to be of order unity. It also can depend on ‘‘chemical interface damping’’ (i. e. transfer of surface plasmon energy into excitation modes of the surface metal-adsorbate complex) [48]. To obtain the parameter  $A$ , we compared our calculations in the dilute limit to experimental data for the extinction spectra of DNA-linked gold dispersed colloids [9], choosing the parameter  $A$  as the best fitted value, as further discussed below.

Since we are treating disordered clusters, we believe that the best choice for  $\alpha$  is eq. (13), and have used this equation in our calculations. For this choice, the DDA calculation has been compared to a more accurate method [49] for calculating the extinction coefficient for a compact spherical aggregate of 89 30-nm gold nanospheres in an aqueous medium. The DDA result was found to be reasonably consistent with this more accurate method [16]. Also, for a 40-sphere DLA fractal cluster, Mackowski [50] has compared the exact total cross section, as obtained using a multiple scattering formalism, to that obtained from the dipole method in combination with eq. (13), using various choices for the sphere index of refraction. The calculated DDA results agree qualitatively with the exact multiple-scattering calculation, except for a single discrepancy, which can be corrected by adding a frequency-independent constant to the extinction coefficient.

To improve the statistics, we average the calculated  $C_{ext}$  for each cluster over possible orientations. We then sum the averaged extinction coefficients of all the individual clusters to obtain the total extinction coefficient of the suspension. This method should be adequate so long as the total volume fraction of clusters in the suspension is small (dilute regime).

#### IV. NUMERICAL RESULTS

We turn now to our numerical results, based on this approach to modeling the structural and optical properties of gold/DNA composites. We begin with the structural properties.

First, we show that our numerical algorithm does indeed generate an RLCA cluster at  $p_{eff} = 1$ . In Fig. 1, we

show the radius of gyration  $R_g$  for such a cluster, plotted as a function of  $N_m$ .  $R_g$  is defined by the relation

$$R_g^2 = \frac{1}{N_m} \sum_{i=1}^{N_m} |\mathbf{r}_i - \bar{\mathbf{r}}|^2, \quad (17)$$

where  $\mathbf{r}_i$  is the position of the  $i^{th}$  monomer and  $\bar{\mathbf{r}} = N_m^{-1} \sum_i \mathbf{r}_i$  is the cluster center of mass.  $d_f$  is then given by

$$d_f = \lim_{R_g \rightarrow \infty} \frac{d \ln N_m}{d \ln R_g}. \quad (18)$$

Fig. 1 shows that the log-log plot of  $N_m$  against  $R_g$  is indeed a straight line with a slope  $d_f = 2.1$ , consistent with expectations for RLCA, provided  $N_m$  exceeds about 200.

Next, we consider how the radius of gyration  $R_g$ , and hence the fractal dimension of the clusters, varies with  $N_{MC}$ . In Fig. 2, we plot  $R_g$  as a function of the number of MC steps  $N_{MC}$ , for probability  $p_{eff} = 0.9$ . We consider the evolution of clusters having  $N_m$  varying from 100 to 600. In several cases, the final result of the evolution is more than one cluster; in these cases, we calculate  $R_g$  for the largest cluster. As shown in Fig. 2, as the restructuring of cluster proceeds with increasing  $N_{MC}$ , the radius of gyration  $R_g$  of the largest cluster of the system becomes smaller and eventually relaxes to a saturated value.

To characterize these changes, we calculate the fractal dimension  $d_f$  at the beginning of the simulation, and after the system has fully relaxed. In Fig. 3, we show log-log plots of  $R_g(N_m)$  for two different values of  $N_{MC}$ , using the data of Fig. 2. For small  $N_{MC}$  ( $N_{MC} = 100$ ), we measure  $d_f \sim 2.1$ , as expected for an RLCA cluster. But when we measure the value  $d_f$  for the saturated  $R_g$  at large  $N_{MC}$ , we find  $d_f \sim 3$ , corresponding to compact, non-fractal clusters. Thus, the clusters are becoming more compact with increasing simulation time.

In Fig. 4, we show some typical cluster morphologies corresponding to the procedure described above. In Fig. 4(a)-(c), we show a cluster with  $N_m = 1000$ , at  $p = 0.9$ , after 0, 7000, and 70000 MC steps. The gradual transition from a fractal morphology to a more compact one is evident in the figure. (This behavior can also be observed at  $p = 0.95$  although the saturation time is longer than at  $p = 0.90$ .) Also during the simulation, we observe that most configurations have one large cluster and a few monomers as can be seen in Fig. 4 (b) and (c). This indicates that at large  $p_{eff}$  the mechanism for cluster restructuring is mainly the diffusion of monomers along the surface of the large cluster.

From these numerical results we may infer some qualitative conclusions about the sol-gel transition mentioned earlier. We denote by  $\tau_1$  the time needed to break one monomer from the surface of a large cluster. We estimate this time as  $\tau_1 \propto \tau_0/(1 - p_{eff})^{N_{av}}$ , where  $\tau_0$  is the

time needed to break a single link between two particles, and  $N_{av}$  is the average number of links on one monomer at the surface of a large cluster. Thus  $\tau_1$  diverges as  $p_{eff} \rightarrow 1$ , but is finite for any  $p_{eff} < 1$ , allowing the largest cluster to relax to a non-fractal structure. Hence, we can expect that  $p_{SG}$  should be close to 1, if sufficient relaxation time is provided.

Next, we turn to the calculated optical properties of these gold nanoparticle/DNA composites, based on this structural model. We begin by showing in Fig. 5 the computed extinction coefficients as a function of  $\lambda$  for gold monomers with 6.5 nm radius, including the quantum size corrections embodied in eqs. (11), (13), (15), and (16). For comparison, we also show  $C_{ext}(\lambda)$  with no quantum size correction, and the experimental data in Storhoff, *et al.* [9]. The rather sharp extinction peak near  $\lambda = 530$  nm corresponds to the well-known surface plasmon peak, in which light is absorbed by an oscillation of the electronic charge within the gold nanoparticle. We find that the quantum-size-corrected extinction coefficients give the best fit to the experimental data if we choose  $A = 0.85$ . This value is of order unity, as expected.

We now discuss the optical properties of various clusters. In Fig. 6, we show the specific extinction coefficient  $C_{ext}(\lambda)/L^3$ , as calculated using the DDA for clusters of gold monomers of radius 20 nm, arranged on a simple cubic lattice of edge varying from  $L = 1$  to  $L = 7$  lattice constants, and thus from  $N_m = 1$  to  $N_m = 343$ . We choose the lattice constant  $\ell = 48$  nm. For  $L = 1$ , the extinction coefficient corresponds to a single monomer. As  $L$  increases, the peak first shifts towards the infrared, then broadens substantially.

In Fig. 7, we show  $C_{ext}(\lambda)/N_m$  as a function of  $\lambda$  for  $N_m$  varying from 1 to 343, but with particles now forming a single RLCA cluster. Once again, the particles have radius 20 nm as in Fig. 6, and the RLCA cluster forms on a simple cubic lattice of the same lattice constant  $\ell = 48$  nm. The cluster is generated using the RLCA algorithm described at the beginning of Sec. IIB. As in Fig. 6, the extinction peak is red-shifted and broadened as  $N$  increases, but both the shift and the broadening are *substantially smaller* than in Fig. 6.

As a final comparison, we show in Fig. 8 the specific extinction coefficients  $C_{ext}(\lambda)/N_m$  for the *fully relaxed* configurations generated by the algorithm of Section IIB. We set  $p_{eff} = 0.9$  and consider  $N_m$  varying from 1 to 400, as indicated in the legend. The behavior of  $C_{ext}$  in this case resembles Fig. 6 more than Fig. 7; in particular, the surface plasmon peak is more broadened and red-shifted than that of Fig. 7. This result is not surprising, since the clusters of Fig. 8, like those of Fig. 6 and unlike those of Fig. 7, are compact and non-fractal, though they incorporate some disorder.

Figs. 6 and 8 show that compact, non-fractal clusters (whether regular or irregular) have similar optical prop-

erties. Now, these clusters do have various structural differences; for example, the clusters of Fig. 8 have rougher surfaces than those of Fig. 6. We conclude that these structural differences do not significantly affect the cluster extinction coefficients. Of the three extinction coefficients shown in Figs. 6-8, that of Fig. 7 agrees best with experiment; those of Figs. 6 and 8 show too large a broadening and red shift of the surface plasmon peak.

In Fig. 9, we show the calculated normalized extinction coefficient  $C_{ext}(\lambda)/N_m$  at fixed wavelength  $\lambda = 520$  nm as a function of  $p_{eff}$ . The three continuous curves represent the results of the model described in our previous paper [18]; In this model, the cluster is constructed starting from a simple cubic lattice of linear dimension  $L\ell$ , fully occupied by monomers of radius  $a$ . Bonds are then removed with probability  $1 - p_{eff}$ . At a given value of  $p_{eff}$ , there are one or more clusters, depending on the relation of  $p_{eff}$  to the bond percolation threshold  $p_c$  and on  $L$ . The open circles represent the result of the model of this paper - that is, the final cluster is the result of a series of MC steps, each consisting of an RLCA aggregation, followed by a thermally induced breakup of the cluster. The calculated  $C_{ext}(\lambda)/N_m$  are based on the long-time and thus relaxed configurations generated by this procedure.

As is evident from Fig. 9, there is a sharp drop in  $C_{ext}(\lambda)/N_m$  at a characteristic value of  $p_{eff}$  in both models, which we identify with the melting transition for that model. For the bond percolation model of Ref. [18], the melting value  $p_M$  is close to 0.25, the bond percolation threshold on a simple cubic lattice in  $d = 3$ . For the model of the present paper, the melting point  $p_M$  occurs at a considerably higher value of  $p_{eff}$ . In the present model, unlike the previous model of Ref. [18], the final cluster results from many steps of link removal and reformation. Thus the infinite cluster which is formed from the percolation model, can not survive at the bond percolation threshold because it contains many weak links which will break apart after several link removal steps. Thus, there should be an *increase* in the melting value of  $p_M$ , as observed in our simulations.

In Fig. 4 (d), we illustrate a typical configuration generated at  $p_{eff} = 0.6$  by the present model. Here we can clearly see that there is no large cluster, even though the  $p_{eff}$  is much higher than the bond percolation threshold  $p_c$ .

Even though the value of  $p_M$  at melting is larger for the present model than in our previous model in Ref. [18], the *sharpness* of the melting transition (as seen in the calculated optical properties) is similar to that found previously. The reason is that the sharp transition results mainly from the individual link properties [cf. eq. (3)], not the behavior of the cluster. Thus, the present model preserves the sharp melting transition reported in experiments [20,22].

In Fig. 10, we replot the results of Fig. 9, but with

$p_{eff}$  translated into a temperature using the prescription of eqs. (2) and (3). The higher melting value of  $p_{eff}$  obtained from the present model now translates into a lower melting temperature  $T_M$ , in comparison to the percolation model in Ref. [18].

A striking feature of Figs. 9 and 10 is the “rebound effect,” seen in the cross and square of Fig. 9, and in the cross in Fig. 10. The square at  $p_{eff} = 1$  in Fig. 9 represents the calculated  $C_{ext}(\lambda)/N_m$  resulting from pure RLCA. The cross at  $p_{eff} = 0.9$  in Fig. 9 or in Fig. 10 represents a configuration obtained after 7000 MC steps, which is not long enough to produce the asymptotic compact cluster for this process at this value of  $p_{eff}$ . In both cases,  $C_{ext}(\lambda)/N_m$  is larger than that of the fully relaxed configuration for this  $p_{eff}$ . This behavior can be understood quite simply. Since these points are not fully relaxed, they correspond to clusters which are more fractal than the fully relaxed clusters. Being more fractal, they show some characteristics of the melted clusters at this wavelength; hence, they have a somewhat higher  $C_{ext}(\lambda)/N_m$  than the fully relaxed samples. In fact, this rebound effect has been observed in experiments which are carried out on gold/DNA aggregates [4,9,17,20,22]. However, when gold/DNA composites are formed in the presence of a DNA-coated flat surface, this effect was not observed [20].

The observation of the rebound effect in some experiments but not in others needs to be understood, as does our result that among the three extinction coefficients shown in Figs. 6-8, that of Fig. 7, which represents the fractal aggregate, agrees best with experiment. Both results suggest that fractal-like gel state persists up to surprisingly high temperatures, such as room temperature. On the other hand, our numerical study of our structural model suggests that  $p_{SG}$  is either 1 or at least close to 1, given a sufficiently long relaxation time, which implies that a gel state should exist only at very low temperatures at such long times. We will discuss both of these questions in the next section.

## V. DISCUSSION AND CONCLUSIONS

In this paper, we have described a structural model for the formation of gold/DNA nanocomposites, going well beyond our earlier, purely percolation model. The model includes several key features expected to play a role in these aggregates. For example, we include both the formation of clusters via reaction-limited cluster-cluster aggregation, and the thermally induced dehybridization which breaks up the links between the gold monomers. We also calculate the aggregate extinction coefficient  $C_{ext}(\lambda)$  for some of the model structures.

Our structural model is characterized by two types of transitions. The first is the melting transition mentioned above. Above  $p_M$ , in the limit of a large number

of monomers, the system is characterized by at least one large cluster; below  $p_M$ , this cluster breaks up into two or more smaller clusters. In our previous percolation model,  $p_M$  coincides with the percolation threshold, but in the present model, it occurs at a higher value of  $p_{eff}$ . It is observable as a rather sharp transition in  $C_{ext}(\lambda)$  at a characteristic wavelength of about 520 nm. The other transition is the sol-gel transition. For  $p > p_{SG}$ , the aggregate has a fractal gel-like structure, while for  $p < p_{SG}$ , it is a non-fractal sol. We have presented some numerical evidence showing that this sol-gel transition will occur at  $p_{eff} \sim 1$ , if the sufficient relaxation time is provided.

However, our calculated  $C_{ext}(\lambda)$  agree best with experiment if we assume that the composites grow into a fractal gel-like structure, rather than the compact sol structure. Specifically, the surface plasmon peak seen in  $C_{ext}(\lambda)$  for isolated gold monomers is broadened and red-shifted by about the right amount, in comparison to experiment, for the fractal clusters, but by far too much for the compact, non-fractal clusters.

Thus, it appears that the full restructuring of our model, which would eventually give rise to a non-fractal, does not go to completion in the experimental composites. There are various possible reasons for this behavior. Most likely, the time required for a full relaxation is simply too long. If the composite is well below its melting temperature, only a small fraction of links are broken and the relaxation is likely to be very slow. As an illustration, we found that, for  $p_{eff} = 0.9$ , even  $N_{MC} = 7000$  is not long enough to produce the relaxation necessary to generate a non-fractal cluster.

Another suggestive piece of experimental evidence is the rebound effect. According to our calculations,  $C_{ext}(\lambda)$  should show a characteristic increase at  $\lambda = 520$  nm, above its fully relaxed value, when the cluster is relaxed for only  $N_{MC} = 7000$  steps. With this increase,  $C_{ext}(\lambda)$  is slightly larger than the fully relaxed value expected at this  $\lambda$  for a non-fractal cluster. Experiments do indeed show indications of this rebound effect [4,9,17,20,22].

In summary, we have presented a model for the structural evolution of gold/DNA composites. This model leads to a wide range of structures which depend on the characteristic parameters of the model: the number of monomers, the simulation time, and the temperature. The optical properties of these composites calculated from the resulting structure are consistent with experiment. In particular, we obtain the observed sharp melting transition with a characteristic dependence on monomer radius, a characteristic shift and broadening of the surface plasmon peak in the extinction, of about the experimental magnitude, and a characteristic rebound in  $C_{ext}(\lambda)$ , which indicates that the restructuring of the experimental composites has not been able to go to completion. In view of these successes, we plan to extend the present work to study the sol-gel transition in gold/DNA



nanocomposites. The results of this investigation will be described in a future publication [51].

## VI. ACKNOWLEDGMENTS

This work has been supported by grant NSF DMR01-04987, and by an Ohio State University Postdoctoral Fellowship. Calculations were carried out using the facilities of the Ohio Supercomputer Center. We thank Prof. M. Kardar, Prof. C. H. Kiang, Prof. D. R. Nelson, and Prof. D. A. Weitz for valuable discussions; SYP also thanks Prof. M. Kardar for his kind hospitality during the stay in MIT.

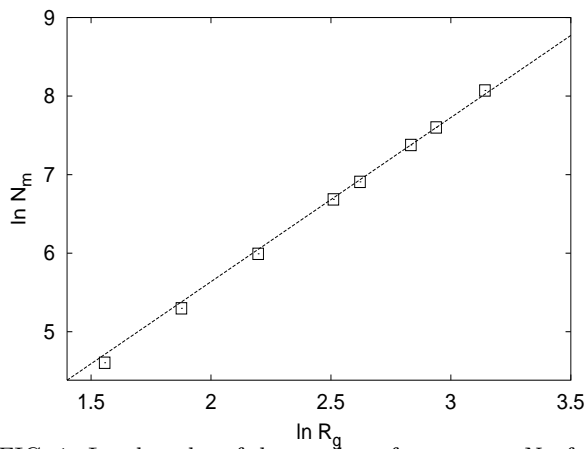


FIG. 1. Log-log plot of the number of monomers  $N_m$  for an RLCA cluster at  $p_{eff} = 1$ , plotted as a function of the radius of gyration  $R_g$ . Squares: present calculations; dashed line: least squares fit. The slope of the dashed line is  $2.1 = d_f$ , consistent with expectations for RLCA clusters in  $d = 3$ .

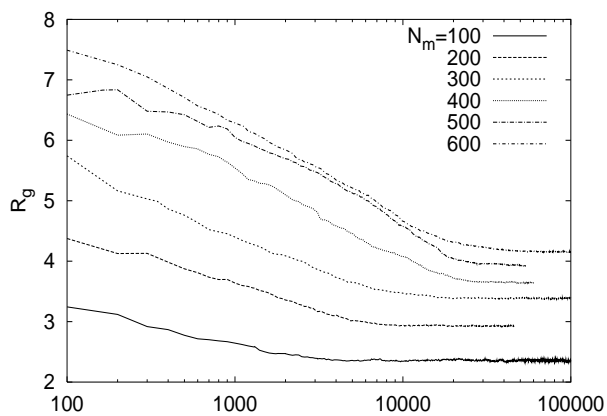


FIG. 2. Variation of  $R_g$  with number of Monte Carlo steps  $N_{MC}$ , as obtained using the algorithm described in the text for probability  $p_{eff} = 0.9$ , and clusters with a number of monomers  $N_m$  varying from 100 to 600, as indicated.

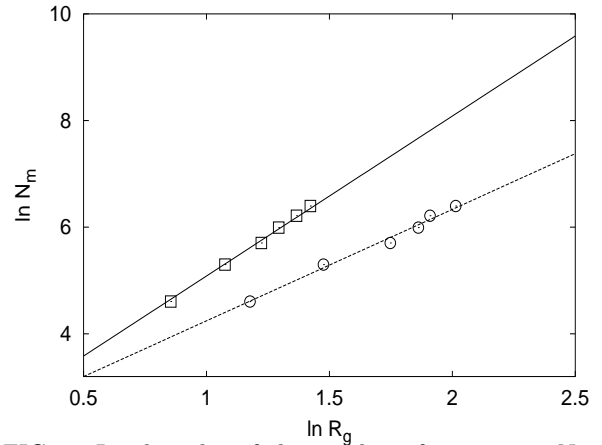


FIG. 3. Log-log plot of the number of monomers  $N_m$  for the clusters generated by the algorithm described in the text, at  $p_{eff} = 0.9$ , as a function of the radius of gyration  $R_g$ . The open circles represent the data of Fig. 2 for  $N_m$  as a function of  $R_g$  at  $N_{MC} = 100$ . The slope of dashed line is 2.1, the expected value for RLCA. The open squares represent the relaxed values of  $R_g$  for large  $N_{MC}$ , also taken from Fig. 2. They are well fitted by the solid line, which has a slope of 3.0, corresponding to a compact, non-fractal cluster.

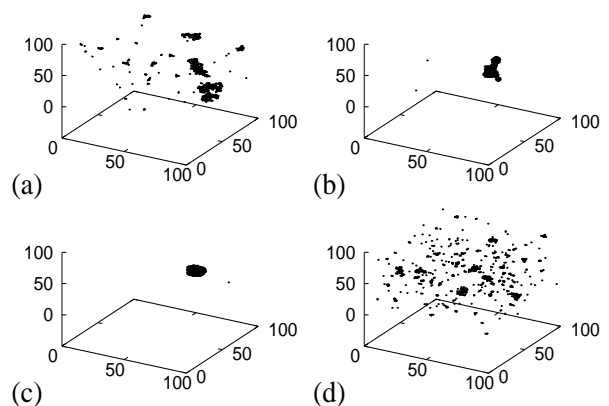


FIG. 4. (a) Initial form of the cluster, after the first reaction-limited aggregation ( $N_{MC} = 0$ ), for  $N_m = 1000$ ,  $p = 0.9$ . The clusters are divided from an RLCA fractal, with fractal dimension  $d_f \sim 2.1$ . (b). Same cluster, but after 7000 Monte Carlo steps. (c) Same as (b), but after 70000 Monte Carlo steps (nearly saturated). (d). Clusters with  $p = 0.6$ ,  $N_m = 1000$ , and  $N_{MC} = 6000$ .

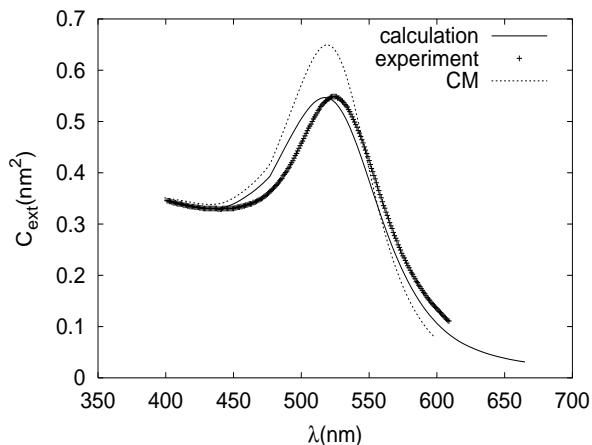


FIG. 5. Extinction coefficient  $C_{ext}(\lambda)$  per unit volume of gold for a dilute suspension of gold nanoparticles in water, plotted for a particle radius  $a = 6.5$  nm. Crosses: experimental data of Ref. [9]. Full curve: calculated extinction coefficient including quantum size corrections, as computed from eqs. (15) and (16) with  $A = 0.85$ . Dashed line: calculated extinction coefficient without quantum size corrections.

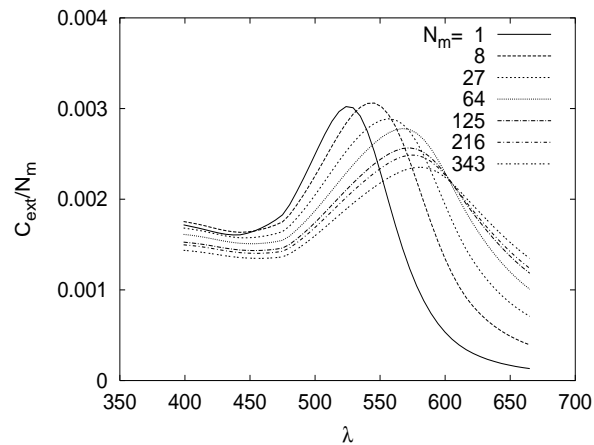


FIG. 7.  $C_{ext}(\lambda)/N_m$  plotted as a function of  $\lambda$  for various number of particles  $N_m$  from 1 to 343. In all cases, we assume the cluster forms a RLCA cluster with particles of radius 20 nm, and is generated on a lattice with lattice constant  $\ell = 48$  nm.  $C_{ext}(\lambda)$  is calculated using the DDA as in Fig. 5.

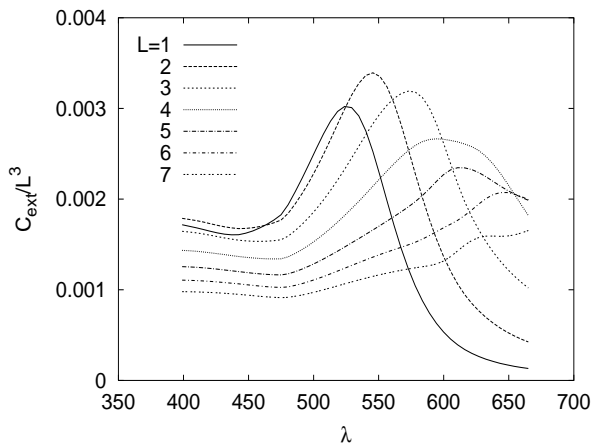


FIG. 6.  $C_{ext}(\lambda)/L^3$  plotted as a function of  $\lambda$  for  $L \times L \times L$  clusters with edge varying from  $L = 1$  to  $L = 7$  lattice constants. In all cases, we assume the cluster forms a cubic compact cluster with particles of radius 20 nm, lattice constant  $\ell = 48$  nm; so the number  $N_m$  of monomers varies from 1 to 343. We use the DDA including quantum size corrections from eqs. (15) and (16) and polarizability obtained from eqs. (10), (11), (13), and (14)

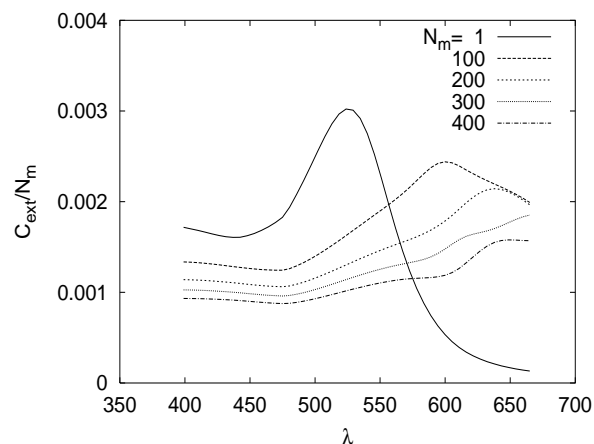


FIG. 8.  $C_{ext}(\lambda)/N_m$  plotted as a function of  $\lambda$  for a number  $N_m$  of monomers varying from 1 to 400. In all cases, we use relaxed configurations from the algorithm in the text, whose radii of gyration are shown in Fig. 2. (Examples of these configurations are shown in Fig. 4.) Once again, we assume a monomer radius is 20 nm, a lattice constant of 48 nm, and use the same algorithm as in Figs. 5 and 6 to calculate the extinction coefficient.

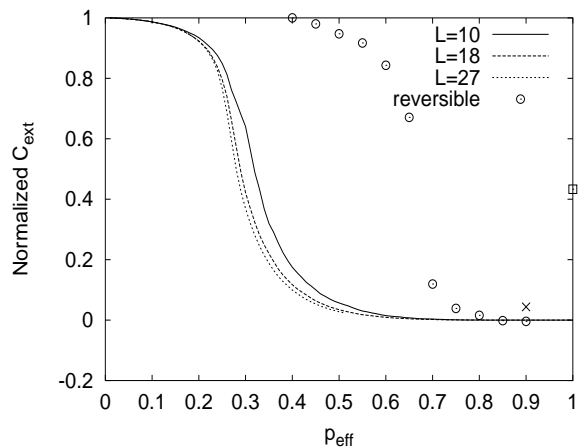


FIG. 9. Normalized  $C_{ext}(\lambda)$  at a fixed wavelength of  $\lambda = 520$  nm, as calculated in the DDA, for clusters of various geometries and different numbers  $N_m$  of monomers of radius 20 nm, plotted as a function of  $p_{eff}$ . Full curves: clusters generated by percolation model of Ref. [18];  $p_{eff}$  represents the fraction of links which are present in this model. The total number of monomers is  $L^3$ . Open circles:  $C_{ext}$  at  $\lambda = 520$  nm for the model of the present paper, with  $N_m = 1000$ , with fully relaxed long-time configurations. The square at  $p_{eff} = 1.0$  represents the calculated  $C_{ext}$  at  $\lambda = 520$  nm assuming RLCA clusters. Cross at  $p_{eff} = 0.9$  represent the calculated values of  $C_{ext}$  at  $\lambda = 520$  nm for the unsaturated configuration obtained after  $N_{MC} = 7000$  steps; the cross at  $p_{eff} = 1$  is the value of  $C_{ext}$  obtained after a single RLCA aggregation.

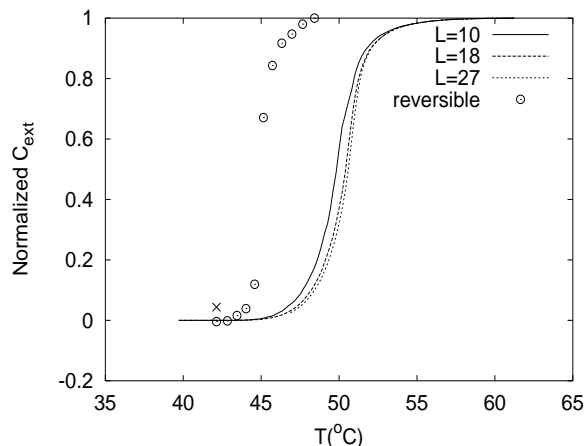


FIG. 10. Same as Fig. 8, but with  $p_{eff}$  translated into a temperature, using eqs. (2) and (3). The cross corresponds to  $p_{eff} = 0.9$  after  $N_{MC} = 7000$ .

[1] C. F. Bohren and D. R. Huffman, *Absorption and Scattering of Light by Small Particles*, (John Wiley & Sons,

New York, 1983).

[2] U. Kreibig and M. Vollmer, *Optical Properties of Metal Clusters*, (Springer-Verlag, Berlin, 1995).

[3] C. Sanchez, G. J. de A. A. Soler-Illia, F. Ribot, T. Lalot, C. R. Mayer, and V. Cabuil, *Chem. Mater.* **13**, 3061 (2001).

[4] C. A. Mirkin, R. L. Letsinger, R. C. Mucic, J. J. Storhoff, *Nature* **382**, 607 (1996).

[5] A. P. Alivisatos, K. P. Johnsson, X. Peng, T. E. Wilson, C. J. Loweth, M. P. Bruchez Jr., and P. G. Schultz, *Nature* **382**, 609 (1996).

[6] E. Winfree, F. Liu, L. A. Wenzler, and N. C. Seeman, *Nature* **394**, 539 (1998).

[7] D. Zanchet, C. M. Michel, W. J. Parak, D. Gerion, and A. P. Alivisatos, *Nano Lett.* **1**, 32 (2001).

[8] D. R. Nelson, *Nano Lett.* **2**, 1125 (2002).

[9] R. Elghanian, J. J. Storhoff, R. C. Mucic, R. L. Letsinger, and C. A. Mirkin, *Science* **277**, 1078 (1997); J. J. Storhoff, R. Elghanian, R. C. Mucic, C. A. Mirkin, R. L. Letsinger, *J. Am. Chem. Soc.* **120**, 1959 (1998).

[10] M. Bruchez Jr., M. Moronne, P. Gin, S. Weiss, and A. P. Alivisatos, *Science* **281**, 2013 (1998).

[11] W. C. W. Chan and S. Nie, *Science* **281**, 2016 (1998).

[12] T. A. Taton, C. A. Mirkin, and R. L. Letsinger, *Science* **289**, 1757 (2000).

[13] S.-J. Park, T. A. Taton, and C. A. Mirkin, *Science* **295**, 1503 (2002).

[14] Y. C. Cao, R. Jin, and C. A. Mirkin, *Science* **297**, 1536 (2002).

[15] A. A. Lazarides and G. C. Schatz, *J. Phys. Chem. B* **104**, 460 (2000), and references cited therein.

[16] A. A. Lazarides and G. C. Schatz, *J. Chem. Phys.* **112**, 2987 (2000), and references cited therein.

[17] J. J. Storhoff, A. A. Lazarides, R. C. Mucic, C. A. Mirkin, R. L. Letsinger, and G. C. Schatz, *J. Am. Chem. Soc.* **122**, 4640 (2000).

[18] S. Y. Park and D. Stroud, *Phys. Rev. B* **67**, 212202 (2003).

[19] S. Y. Park and D. Stroud, *Physica B* (in press).

[20] R. C. Jin, G. S. Wu, Z. Li, C. A. Mirkin, and G. C. Schatz, *J. Am. Chem. Soc.* **125**, 1643 (2003).

[21] K. Drukker, G. Wu, and G. C. Schatz, *J. Chem. Phys.* **114**, 579 (2001).

[22] C.-H. Kiang, *Physica A* **321**, 164 (2003).

[23] M. Y. Lin, H. M. Lindsay, D. A. Weitz, R. C. Ball, R. Klein, and P. Meakin, *Phys. Rev. A* **41**, 2005 (1990).

[24] P. Meakin, *Adv. Colloid Interf. Science* **28**, 249 (1988), and references cited therein.

[25] T. Terao and T. Nakayama, *Phys. Rev. E* **58**, 3490 (1998).

[26] V. A. Bloomfield, D. M. Crothers, and I. Tinoco Jr., *Nucleic Acids* (University Science Books, Sausalito, California, 2000).

[27] In reality,  $\tau_{bind}$  will not remain unchanged as the aggregation proceeds, because the number of aggregation attempts depends on the number of clusters at a given stage of the simulation. This number become smaller as aggregation proceeds. We do not consider this effect in our simulations.

[28] For the details of RLCA, see, e. g., Ref. [24], or P. Meakin, *Adv. Colloid Interf. Science* **28**, 249 (1988).

- [29] This sol-gel transition may be an example of the “jamming transition” discussed by Trappe *et al* [V. Trappe, V. Prasad, L. Cipelletti, P. N. Segre, and D. A. Weitz, *Nature* **411**, 772 (2001)], which occurs in systems of particles with attractive interactions.
- [30] See, e. g., D. Stauffer and A. Aharony, *Introduction to Percolation Theory, 2nd Edition* (Taylor and Francis, London, 1994).
- [31] H. Werntges, G. Steger, D. Riesner, and H.-J. Fritz, *Nucleic Acids Res.* **14**, 3773 (1986).
- [32] S. Mann, W. Shenton, M. Li, S. Connolly, and D. Fitzmaurice, *Adv. Mater.* **12**, 147 (2000).
- [33] A. K. Boal, F. Ilhan, J. E. DeRouchey, T. Thurn-Albrecht, T. P. Russell, and V. M. Rotello, *Nature* **404**, 746 (2000).
- [34] Y. Kim, R. C. Johnson, and J. T. Hupp, *Nano Lett.* **1**, 165 (2001).
- [35] In principle, there should also be a term of the form  $c_2(T - T_M^0)^2$  in this expansion. However, experiments on isolated pairs of DNA molecules appear to be best fit by  $c_2 = 0$ . We have therefore continued to use  $c_2 = 0$  in our treatment of the aggregate melting.
- [36] L. M. Demers, C. A. Mirkin, R. C. Mucic, R. A. Reynolds, III, R. L. Letsinger, R. Elghanian, and G. Viswanadham, *Anal. Chem.* **72**, 5535 (2000).
- [37] E. M. Purcell and C. R. Pennypacker, *Astrophys. J.* **186**, 705 (1973).
- [38] J. J. Goodman, B. T. Draine, and P. J. Flatau, *Opt. Lett.* **16**, 1198 (1991).
- [39] For a review which discusses the proper choice of polarizability and the applicability of the DDA, see, e. g., B. T. Draine and P. J. Flatau, *J. Opt. Soc. Am. A* **11**, 1491 (1994).
- [40] See, e. g., E. M. Purcell, *Electricity and Magnetism*, Berkeley Physics Course, Vol. 2 (McGraw-Hill, New York, 1965).
- [41] B. T. Draine, *Astrophys. J.* **333**, 848 (1988); G. H. Goedecke and S. G. O’Brien, *Appl. Opt.* **27**, 2431 (1988).
- [42] B. T. Draine and J. Goodman, *Astrophys. J.* **405**, 685 (1993).
- [43] W. T. Doyle, *Phys. Rev. B* **39**, 9852 (1989).
- [44] D. W. Lynch and W. R. Hunter, in *Handbook of Optical Constants of Solids*, E. D. Palik, ed. (Academic, New York, 1985), p. 294.
- [45] P. B. Johnson and R. W. Christy, *Phys. Rev. B* **6**, 4370 (1972).
- [46] C. G. Granqvist and O. Hunderi, *Phys. Rev. B* **16**, 3513 (1977).
- [47] For a review discussing the proper choice of the parameter  $A$ , see, e. g. Ref. [2] or S. Link and M. A. El-Sayed, *J. Phys. Chem. B* **103**, 8410 (1999).
- [48] N. J. Persson, *Surf. Sci.* **281**, 153 (1993).
- [49] D. W. Mackowski and M. I. Mishchenko, *J. Opt. Soc. Am. A* **13**, 2266 (1996).
- [50] D. W. Mackowski, *J. Opt. Soc. Am. A* **11**, 2851 (1994).
- [51] S. Y. Park and D. Stroud, (to be published).